inorganics

MDPI

Article

Surface Plasmon Resonance Effect of Noble Metal (Ag and Au) Nanoparticles on $BiVO_4$ for Photoelectrochemical Water Splitting

Rui Liu [1], Difu Zhan [1], Dong Wang [1], Changcun Han [1,*], Qian Fu [1], Hongxun Zhu [1], Zhuxiang Mao [1] and Zhao-Qing Liu [2,*]

[1] College of Science, Hubei University of Technology, Wuhan 430068, China; 18602724029@163.com (R.L.); qq2290695435@outlook.com (D.Z.); wd19971029@gmail.com (D.W.); ludeng9531177yigu@163.com (Q.F.); zhx2zqy@gmail.com (H.Z.); zhm879741871@163.com (Z.M.)

[2] School of Chemistry and Chemical Engineering, Guangzhou University, Guangzhou 510006, China

* Correspondence: hanchangcun@126.com (C.H.); lzqgzu@gzhu.edu.cn (Z.-Q.L.)

Abstract: Photoelectrochemical (PEC) splitting water technology over the years has gradually matured, and now photoanodes loaded with nanoparticles (NPs) show excellent PEC performance. Each of the metal NPs has a different effect on the PEC performance of $BiVO_4$. This work selected the noble metals Ag and Au to modify $BiVO_4$ and study its PEC performance. After recombination, the photocurrent densities of $Ag/BiVO_4$ and $Au/BiVO_4$ photoanodes were 3.88 mA/cm^2 and 1.61 mA/cm^2 at 1.23 V_{RHE}, which were 3.82 and 1.72 times that of pure $BiVO_4$. The hydrogen evolution of pure $BiVO_4$ is about 1.10 $\mu mol \cdot cm^{-2}$. $Ag/BiVO_4$ and $Au/BiVO_4$ contain 3.56 and 2.32 times pure $BiVO_4$, respectively. Through the research, it was found that the composite noble metal (NM) NPs could improve the PEC properties; this is because NM NPs can introduce a surface plasmon resonance (SPR) effect to increase the concentration and accelerate the separation of carriers. The mechanism of the SPR effect can be explained as NM NPs are excited by light generating "hot electrons", and the hot electrons can directly enter the conduction band (CB) of $BiVO_4$ through an electron transfer mechanism. The potential energy of the Schottky barrier generated by the contact of NM NPs with $BiVO_4$ is smaller than that generated by the SPR effect, which enables the "hot electrons" to be smoothly transferred from the NM NPs to the conduction band of $BiVO_4$ without returning to the NM NPs. $Ag/BiVO_4$ showed higher PEC activity than $Au/BiVO_4$ because of its higher light absorption, photocurrent, and oxygen evolution capacity. It can be seen that loading NM NPs increases the concentration of the carriers while the separation and transfer rates of the carriers are improved. In conclusion, it was concluded from this study that the loading of NM NPs is an effective method to improve the water oxidation kinetics of $BiVO_4$ photoanodes.

Keywords: surface plasmon resonance; $BiVO_4$; photoelectrochemical; water splitting; noble metal

Citation: Liu, R.; Zhan, D.; Wang, D.; Han, C.; Fu, Q.; Zhu, H.; Mao, Z.; Liu, Z.-Q. Surface Plasmon Resonance Effect of Noble Metal (Ag and Au) Nanoparticles on $BiVO_4$ for Photoelectrochemical Water Splitting. *Inorganics* **2023**, *11*, 206. https://doi.org/10.3390/inorganics11050206

Academic Editors: Hicham Idriss and Antonino Gulino

Received: 27 March 2023
Revised: 4 May 2023
Accepted: 6 May 2023
Published: 10 May 2023

1. Introduction

With the energy crisis and environmental pollution becoming increasingly prominent, photoelectrochemical (PEC) splitting water technology, as a new energy conversion technology, is attracting attention and being explored by an increasing number of researchers [1–4]. PEC water splitting can convert solar energy into hydrogen with zero pollution [5]. However, the PEC splitting efficiency is low due to the slow water oxidation process, so finding a photoanode with high activity which responds to visible light is the required basis. There are many semiconductor materials that have been found to be useful as photoanodes, such as WO_3, ZnO, $BiVO_4$, TiO_2, Cu_2O [6–10], etc. Among them, bismuth vanadate ($BiVO_4$) is a promising photoanode semiconductor material. $BiVO_4$ has a suitable band gap of about 2.45 eV and a light absorption range of 300–520 nm. In addition, $BiVO_4$ is cheap, abundant,

and stable in aqueous solution. Therefore, $BiVO_4$ is a very suitable photoanode n-type semiconductor material [11].

However, pure $BiVO_4$ neither achieved the theoretical effect in hydrogen conversion, nor the theoretical photocurrent density of 7.5 mA/cm^2 [12]. This is because pure $BiVO_4$ has the disadvantages of slow electron transfer, low separation rate of photogenerated carriers, rapid recombination of photogenerated carriers, and slow water oxidation kinetics [13]. Many methods have been proposed to solve these problems, such as ion doping, oxygen vacancy, morphology engineering, heterojunction and cocatalysts [14–18]. In addition to these methods, the $BiVO_4$ loading of NM NPs such as Ag and Au is also highly feasible. Geng et al. prepared a composite photoanode, $FeOOH/Au/BiVO_4$, whose photocurrent density is 3.74 times higher than pure $BiVO_4$ [19]. The photochemical (PEC) splitting water property of Au/TiO_2 BNRs photoanode prepared by Su et al. showed high PEC activity [20]. Zhang et al. [21] studied the PEC performance of $BiVO_4$ modified with Au NPs of different sizes. The results showed that the PEC performance of various sizes of modified photoanodes was also different.

This study investigated PEC performance of $BiVO_4$ loaded with noble metal NPs and Ag NPs and Au NPs, NM NPs were investigated, respectively. NM NPs with different concentrations were composited with $BiVO_4$ using hydrothermal and electrodeposition methods, respectively. The PEC performances were greatly improved with the composite NM NPs material, which is mainly due to enhanced conductivity, the surface plasmon resonance (SPR) effect, and the Schottky barrier created by metal-semiconductor contacts. NM NPs are excited by visible light to produce "hot electrons", and "hot electrons" can more easily enter the conduction band (CB) through the electron transfer mechanism, while the Schottky barrier can prevent "hot electrons" from returning to the NM NPs again, which can broaden the light absorption range, increase the carrier concentration, and accelerate the separation and transfer of carriers. The research results show that the composite of Ag NPs and Au NPs with $BiVO_4$ exhibits high PEC activity. This study provides a possible route for noble metal modified semiconductors.

Characterization

The microstructure and surface morphology of the samples were researched by scanning electron microscopy (SEM, Hitachi, SU8010) and transmission electron microscopy (TEM, FEI Company, Tecnai G2 F20). X-ray diffraction (XRD, PANalytical B.V., pyrerea, 20–80°, 10°/min), X-ray photoelectron spectroscopy (XPS, Thermo Fisher Technology, 250Xi, Al-Kα) and energy spectroscopy spectrometry (EDS, FEI Company, EDAX GENESIS) were used to determine the crystal structure, valence states of the elements, and element type in the samples, respectively. The absorption spectra were measured with the diffuse reflectance UV-visible spectra (SHIMADZU UV-2600) over a range of 300–800 nm. Separation and transfer properties of photogenerated charge were investigated by surface photovoltage (SPV, Beijing Perfectlight Technology Co., Ltd., Beijing, China, PLS-SPS1000) and electrochemical impedance spectroscopy (EIS, 5 mV, 0.01 Hz to 100 kHz).

In this paper, the PEC performances of the samples were characterized by the three-electrode electrochemical workstation. The irradiation source for the three-electrode electrochemical workstation consisted of an AM 1.5 G filter and a 300 W Xe lamp. It was detected that the light intensity near the sample surface was about 100 mW/cm^2. Ag/AgCl served as the reference electrode, the sample was the working electrode, and a Pt sheet was used as the counter electrode. The Nernst equation yielded a reversible hydrogen electrode (RHE) result, $E_{RHE} = E_{Ag/AgCl} + 0.1976 + 0.0591pH$ [22].

2. Results and Discussion

The fabrication of $Ag/BiVO_4$ (referring to $Ag_{2.5}/BiVO_4$) and $Au/BiVO_4$ (referring to $Au_{150}/BiVO_4$) is presented in Figure 1. Figure 2 shows the SEM images of $BiVO_4$, $Ag/BiVO_4$, and $Au/BiVO_4$. In Figure 2a, the $BiVO_4$ that was prepared presented a nanochain structure. Nanochains consist of interconnected ellipsoidal nanoparticles; each

nanoparticle is about 250 nm in diameter. Figure 2b shows the schematic diagram of $BiVO_4$ loaded with Ag NPs. Dense and protruding Ag NPs could be observed attached around the chain-like $BiVO_4$. As can be observed in Figure 2c, Au NPs with a diameter of about 5 nm were distributed in a points-like manner on $BiVO_4$. Obviously, NM NPs were successfully combined on $BiVO_4$. It was further observed that there were more Ag NPs than Au NPs on the surface of the composite photoanodes, indicating that Ag NPs modified $BiVO_4$ could provide more active sites.

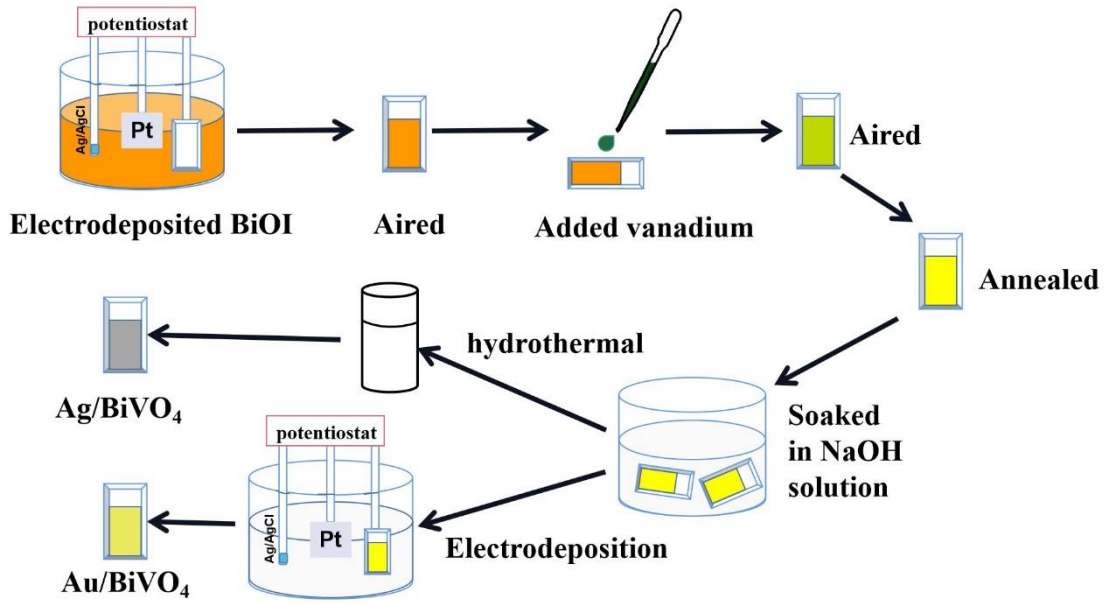

Figure 1. Schematic diagram of the synthesis of photoanode NM/$BiVO_4$.

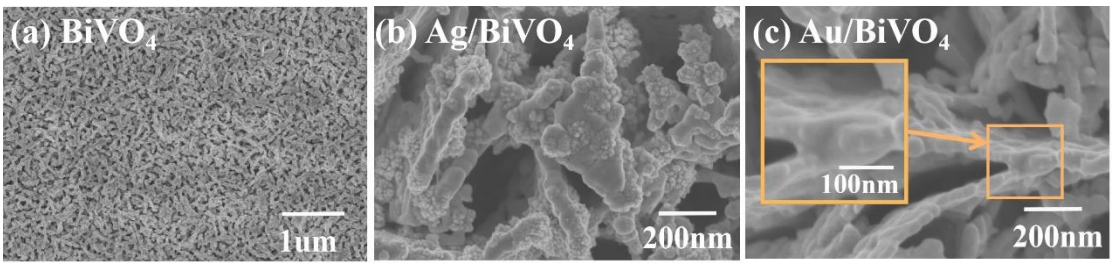

Figure 2. SEM images of (**a**) pure $BiVO_4$, (**b**) Ag/$BiVO_4$, and (**c**) Au/$BiVO_4$.

The surface structure variations obtained were measured by transmission electron microscopy (TEM) and high-resolution transmission electron microscopy (HRTEM) on Ag/$BiVO_4$ and Au/$BiVO_4$ as shown in Figure 3. As presented in Figure 3a,b, NM NPs with a diameter of about 5 nm were composited on $BiVO_4$ and presented an appearance of solid cores, which were randomly distributed on the surface of $BiVO_4$. In Figure 3c,d, the lattice fringe spacing of $BiVO_4$ was 0.30 nm and 0.57 nm, which corresponded to the crystal planes (−1 2 1) and (0 2 0), respectively. The lattice fringe spacings were measured as 0.21 nm and 0.24 nm, which corresponded to the (2 0 0) and (1 1 1) crystal planes of Ag NPs and Au NPs. Figure 4 shows the top view of the element mapping, confirming the existence of various elements (Bi, V, O, Ag, Au, and C).

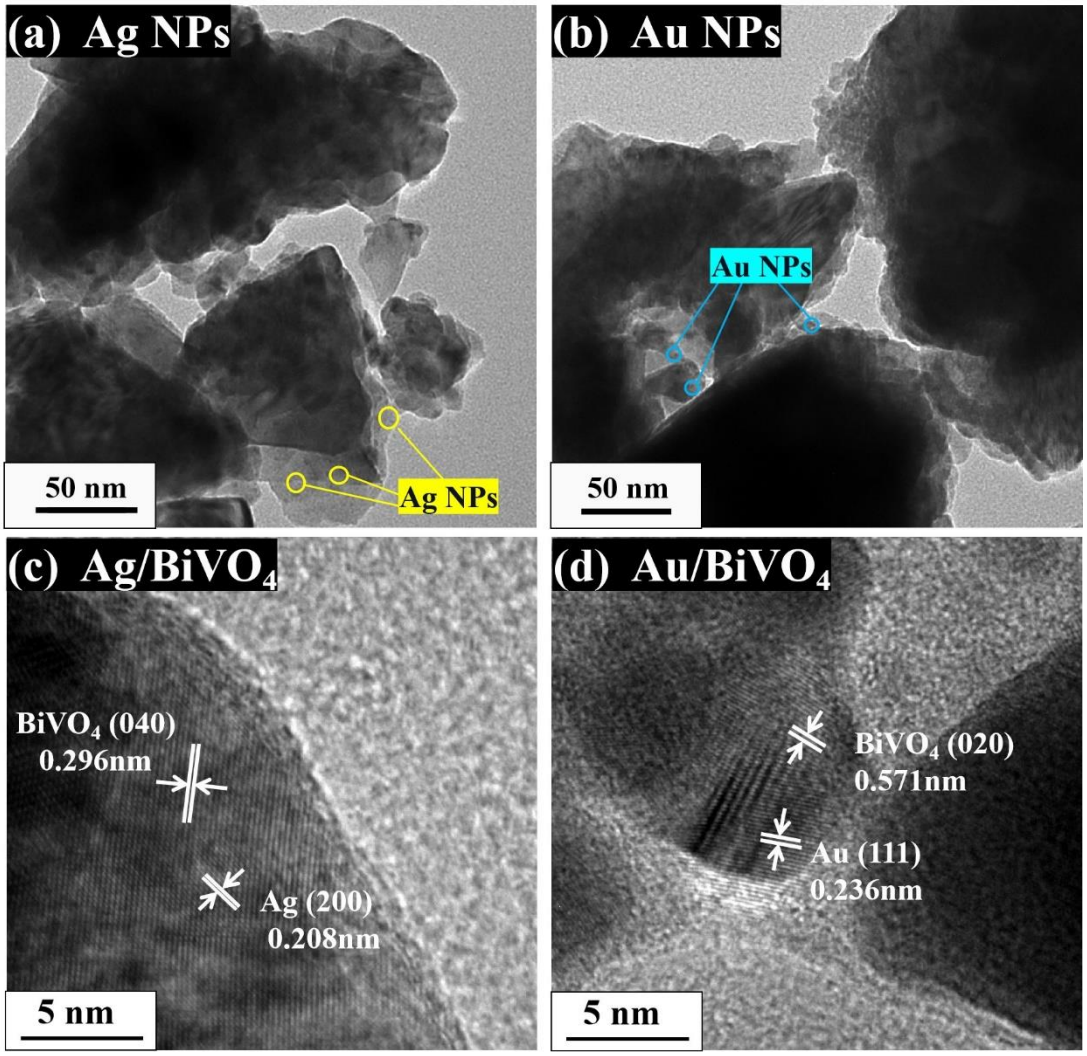

Figure 3. The morphologies of samples were characterized by TEM: (**a**) $Ag/BiVO_4$ and (**b**) $Au/BiVO_4$, while the structures of samples were characterized by HRTEM: (**c**) $Ag/BiVO_4$ and (**d**) $Au/BiVO_4$.

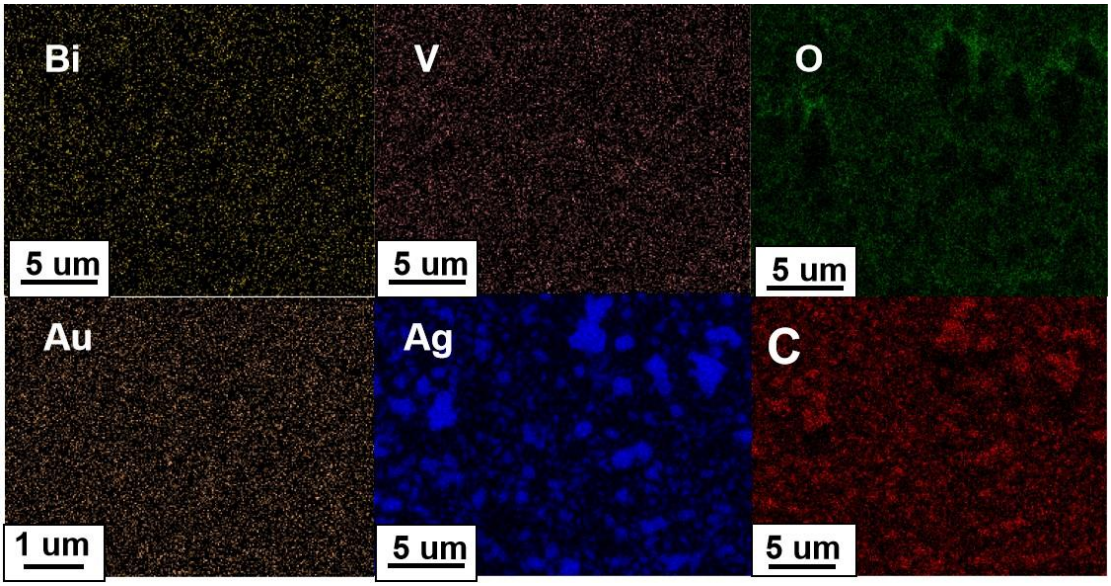

Figure 4. The elements mapping picture of samples.

XRD patterns of $BiVO_4$, $Ag/BiVO_4$, and $Au/BiVO_4$ photoanodes are shown in Figure 5. As presented in Figure 5a, the diffraction peaks of $Ag/BiVO_4$ are located at 28.8°, 30.54°, 35.22°, 38.11°, 44.27°, 64.42°, and 77.47°, of which 28.8°, 30.54°, and 35.22° could match the (−1 2 1), (0 4 0), and (0 0 2) crystal planes of monoclinic $BiVO_4$ (JCPDS NO.14−0688) [23], while 38.11°, 44.27°, 64.42°, and 77.47° could match the (1 1 1), (2 0 0), (2 2 0), and (3 1 1) crystal planes of Ag NPs (JCPDS NO.04-0783). Other peaks could correspond to the peaks of FTO. Figure 5b shows the XRD pattern of the photoanode on Au NP modified $BiVO_4$. Compared to Figure 5c, there are obvious diffraction peaks at 38.18°, 44.39°, 64.58°, and 77.55°. These diffraction peaks correspond to (1 1 1) of Au (JCPDS NO. 04−0784) (2 0 0), (2 2 0), and (3 1 1) crystal planes. The measured diffraction peaks corresponding to Ag NPs and Au NPs have no miscellaneous peaks, which proves that the prepared samples are composite expected zero-valence noble metal nanoparticles.

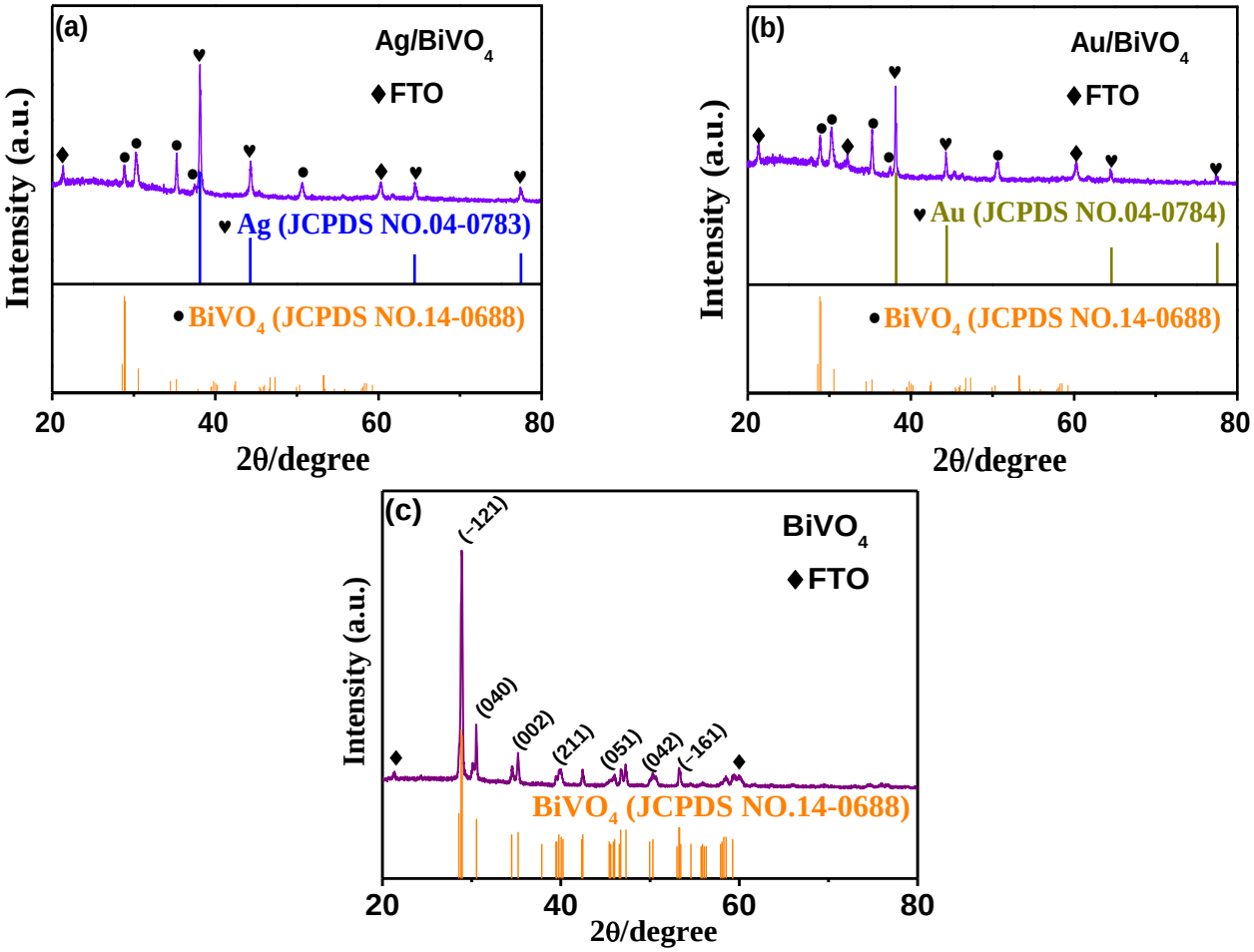

Figure 5. XRD patterns of samples: (**a**) $Ag/BiVO_4$, (**b**) $Au/BiVO_4$, and (**c**) $BiVO_4$.

The surface binding energy characteristics and chemical states of $Ag/BiVO_4$ and $Au/BiVO_4$ photoanodes can be further analyzed by XPS. In this paper, the binding energy of elements was calibrated according to the binding energy standard of C 1s (284.8 eV). Figure 6a shows the binding energies of Bi in $Ag/BiVO_4$ and $Au/BiVO_4$, respectively. The characteristic peaks of Bi^{3+} in $Ag/BiVO_4$ were Bi $4f_{5/2}$ (164.35 eV) and Bi $4f_{7/2}$ (159.05 eV), and in $Au/BiVO_4$ Bi $4f_{5/2}$ (164.67 eV) and Bi $4f_{7/2}$ (159.32 eV). The binding energy of Bi^{3+} in $Ag/BiVO_4$ is smaller than that of $Au/BiVO_4$. In Figure 6b, the characteristic peaks of V^{5+} in $Ag/BiVO_4$ were V $2p_{1/2}$ (524.18 eV) and V $2p_{3/2}$ (516.80 eV), and in $Au/BiVO_4$ V $2p_{1/2}$ (524.30 eV) and V $2p_{3/2}$ (516.95 eV). The binding energies of V $2p_{1/2}$ and V $2p_{3/2}$ in $Ag/BiVO_4$ were 0.12 eV and 0.15 eV, smaller than those of V$2p_{1/2}$ and V $2p_{3/2}$ in $Au/BiVO_4$, respectively. These results proved the existence of $BiVO_4$ [24]. As presented in Figure 5c, the

two peaks at 368.30 eV and 374.30 eV could be attributed to Ag $3d_{5/2}$ and $3d_{3/2}$ spin-orbit components of Ag NPs [25]. As depicted in Figure 6d, peaks of Au $4f_{7/2}$ and Au $4f_{5/2}$ were located at 83.40 eV and 87.05 eV [20]. From the binding energy positions of Bi and V elements in Figure 6a,b, it can be concluded that the electrons of $BiVO_4$ in $Ag/BiVO_4$ are more than those in $BiVO_4$ in $Au/BiVO_4$. This can be explained since the Ag NPs in the $Ag/BiVO_4$ samples generate more hot electrons due to the photoexcited SPR effect which transfer to the conduction band of $BiVO_4$.

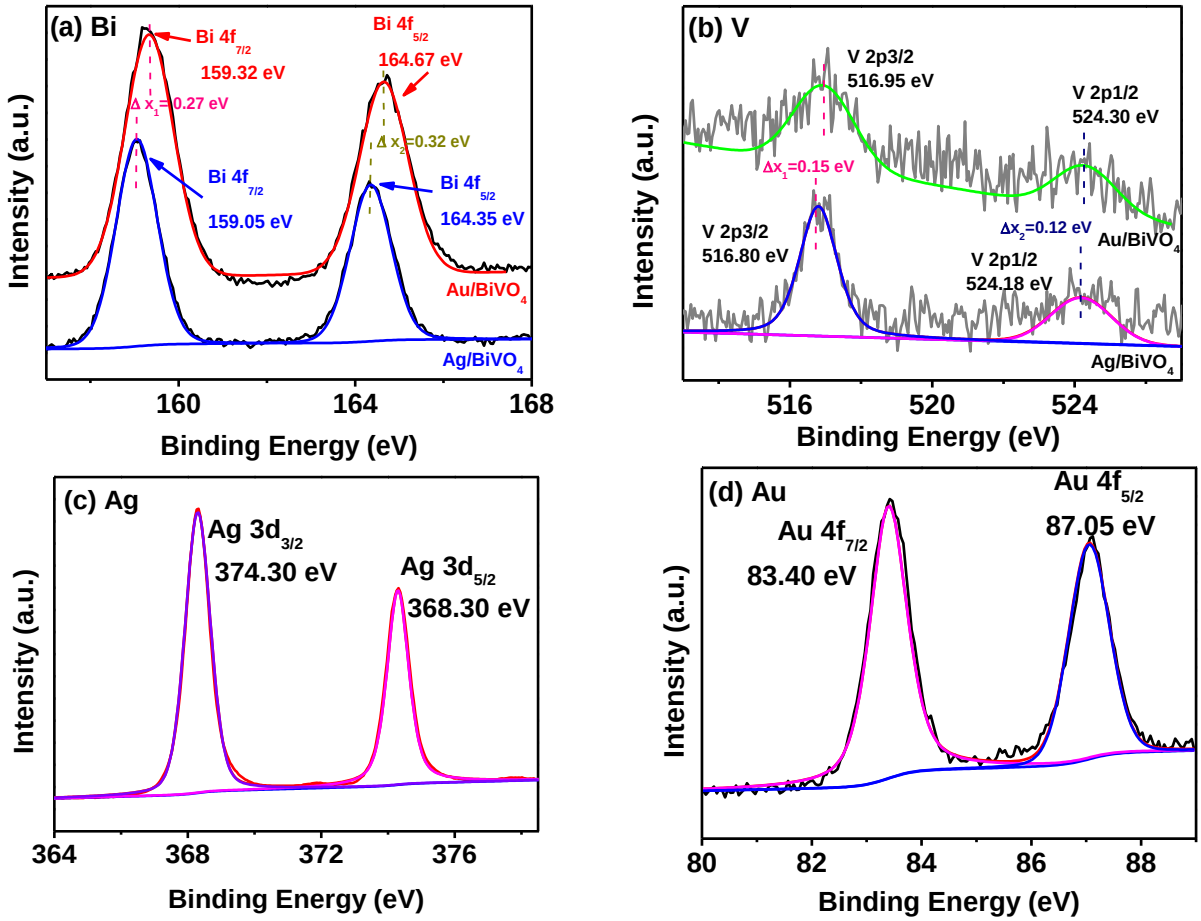

Figure 6. XPS spectrum of various samples of (**a**) Bi, (**b**) V, (**c**) Ag, and (**d**) Au.

Furthermore, the photocurrent density measured is one of the most powerful characterizations of the performance of PEC. The photocurrent densities of $Ag_2/BiVO_4$, $Ag_{2.5}/BiVO_4$, and $Ag_3/BiVO_4$ are characterized in Figure 7a. The results indicate that low or high concentrations of Ag ion solution can decrease the photocurrent. The photocurrent density was maximum at an Ag ion concentration of 2.5 mM. As shown in Figure 7b, the photocurrent density of $Au_{150}/BiVO_4$ has the largest value among $Au_{100}/BiVO_4$, $Au_{150}/BiVO_4$, and $Au_{200}/BiVO_4$. This is because the combination of too many NM NPs produces a metal barrier inside the semiconductor. The formation of this barrier inhibits the electron transport of the semiconductor, which may also lead to the increase of surface recombination; so it is necessary to select the appropriate concentration to modify the semiconductor.

The photocurrent density of $BiVO_4$, $Ag/BiVO_4$, and $Au/BiVO_4$ are shown in Figure 7c. As is theoretically consistent, the photocurrent of pure $BiVO_4$ (0.92 mA/cm^2 at 1.23 V_{RHE}) is the lowest among these. It is obvious that the photocurrent density of $BiVO_4$ loaded with Ag NPs (3.52 mA/cm^2) and Au NPs (1.61 mA/cm^2) was significantly increased at 1.23 V_{RHE}, respectively. The photocurrent densities of $Ag/BiVO_4$ and $Au/BiVO_4$ are 3.52 and 1.72 times that of pure $BiVO_4$, respectively. The photocurrent density of Ag NP modified $BiVO_4$ is higher than that of Au NP modified $BiVO_4$ because Ag NPs can expose

more active sites than Au NPs, and more active sites can absorb carriers more effectively, and transfer more electrons from Ag NPs to the interior of the semiconductor. In order to ensure the stability of the test data, the error bars of data were performed five times, as shown in Figure 8. From the error bar results, it can be concluded that the experimental data are relatively stable. Comparison of the research results of LSV at 1.23V_{RHE} in this paper with previous research results is shown in Table 1. The experimental data in this paper shows a certain improvement compared to previous results. As shown in Figure 7d, under the dark condition, the photocurrent density of the photoanodes is zero. At the beginning of illumination, the circuit quickly generates a peak and undergoes a transient response, then stabilizes. The photocurrent density trend under irradiation is consistent with LSV. From the above results, it can be concluded that the enhancement of photocurrent density is because NM NPs can accelerate both the separation of carriers and the transfer of carriers.

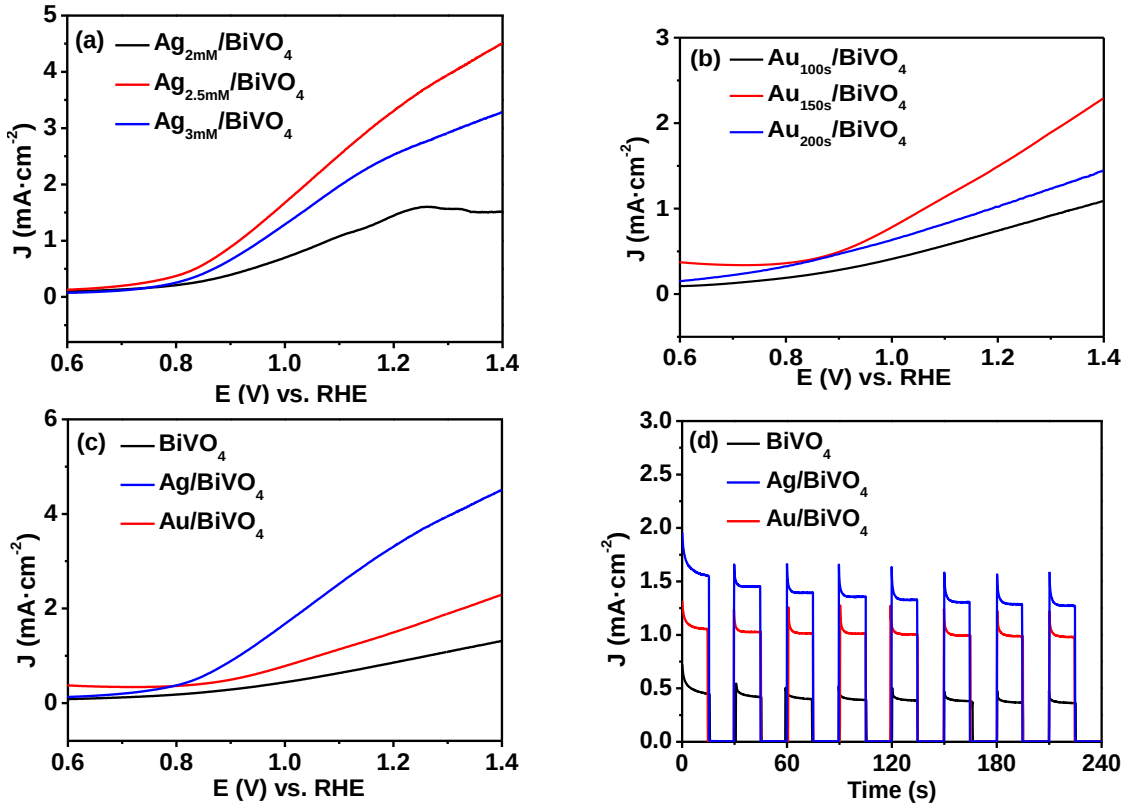

Figure 7. The LSV curves of different concentrations (**a**) Ag NPs, (**b**) Au NPs modified $BiVO_4$, (**c**) the LSV and (**d**) i-t curves of $BiVO_4$, $Ag/BiVO_4$ and $Au/BiVO_4$.

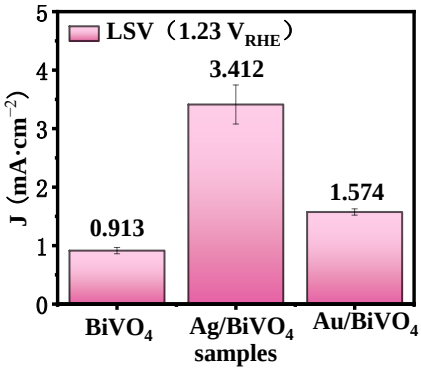

Figure 8. Standard deviation of LSV of the sample tested 5 times at 1.23 V_{RHE}.

Table 1. Comparison of the values of LSV for the present work with previous values of studies based on $BiVO_4$.

Catalyst	LSV (mA/cm^2, 1.23V_{RHE})	Ref.
$Ag/BiVO_4$	3.19	[25]
$Ag/Co_3O_4/BiVO_4$	1.84	[26]
$FeOOH/Au/BiVO_4$	4.64	[19]
$Ag/BiVO_4$	4.1	[21]
$Au/BiVO_4$	1.25	[27]
$Ag/BiVO_4$	3.52	Present work
$Au/BiVO_4$	1.61	Present work

The diffuse reflectance UV-visible spectra (DRS) of $BiVO_4$, $Ag/BiVO_4$, and $Au/BiVO_4$ samples are shown in Figure 9. Pure $BiVO_4$ showed a steep light absorption edge of around 495 nm, and it can be concluded that the band gap of $BiVO_4$ was almost consistent with the theoretical 2.45 eV. When $BiVO_4$ is combined with NM NPs, a slight redshift of the light absorption edge can be found. It is worth noting that $Ag/BiVO_4$ and $Au/BiVO_4$ had obvious absorption peaks around 499 nm and 553 nm due to the SPR effect of Au and Ag [27,28]. Additionally, it can be observed that the intensity and range of the obvious SPR characteristic absorption peak of $Ag/BiVO_4$ are greater than the characteristic absorption peak generated by $Au/BiVO_4$. This could indicate that the SPR effect produced by Ag NPs is stronger than that of Au NPs, and more "hot electrons" can be transferred to $BiVO_4$ to participate in the reaction of PEC splitting of water. Moreover, it can be proved that Ag NPs and Au NPs were successfully loaded on $BiVO_4$. The SPR effect generated by the loading of Ag NPs and Au NPs broadens the absorption of $BiVO_4$ for visible light. It enhances light harvesting, thus improving the solar energy conversion efficiency [29].

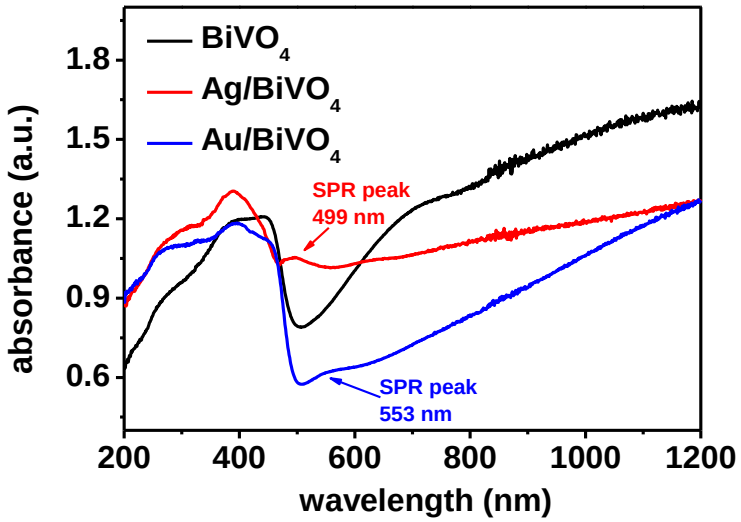

Figure 9. DRS of $BiVO_4$ modified by several noble metal nanoparticles.

The charge separation efficiency of the photoanode can be characterized by PL. PL spectra are displayed in Figure 10a; the PL intensity of pure $BiVO_4$ was the strongest. It can be seen that the recombination rate of photogenerated carriers (electrons and holes) of pure $BiVO_4$ was high. When $BiVO_4$ was loaded with NM NPs, the recombination rate of photogenerated carriers decreased significantly. As anticipated, the test results of PL were consistent with the results of LSV. The recombination rate of photogenerated carriers is as follows: $Ag/BiVO_4$ < $Au/BiVO_4$. The relationship between bias voltage and current density can be explained by ABPE as displayed in Figure 10b. The calculation formula of ABPE is as below [30]:

$$ABPE\ (\%) = I\ (1.23 - V_{RHE})/J_{light}$$

where I, V_{RHE} and J_{light} are the measured photocurrent density (mA/cm^2), the applied bias vs. RHE ($V_{RHE} = V_{Ag/AgCl} + 0.197 + 0.0591pH$), and the light intensity, respectively. The calculation results are as expected, and pure $BiVO_4$ has the lowest ABPE, about 0.027%. The ABPE values of $Ag/BiVO_4$ and $Au/BiVO_4$ are about 0.388% and 0.137%, respectively. In order to ensure the accuracy of the experiment, the value of ABPE at $0.96V_{RHE}$ was analyzed by error bar in Figure 11. In the results of previous studies, it was found that the energy transfer mechanisms in the plasma are as follows: (1) anti-reflection and scattering effects; (2) near-field electromagnetic enhancement; (3) transfer of e^--h^+ pairs between metals and oxides, and (4) plasmon-induced heating [31]. Therefore, it can be determined that the reason for the enhanced PEC performance in this experiment is because of the second and third points mentioned above—the electrical conductivity of metals and the SPR effect of Ag NPs and Au NPs.

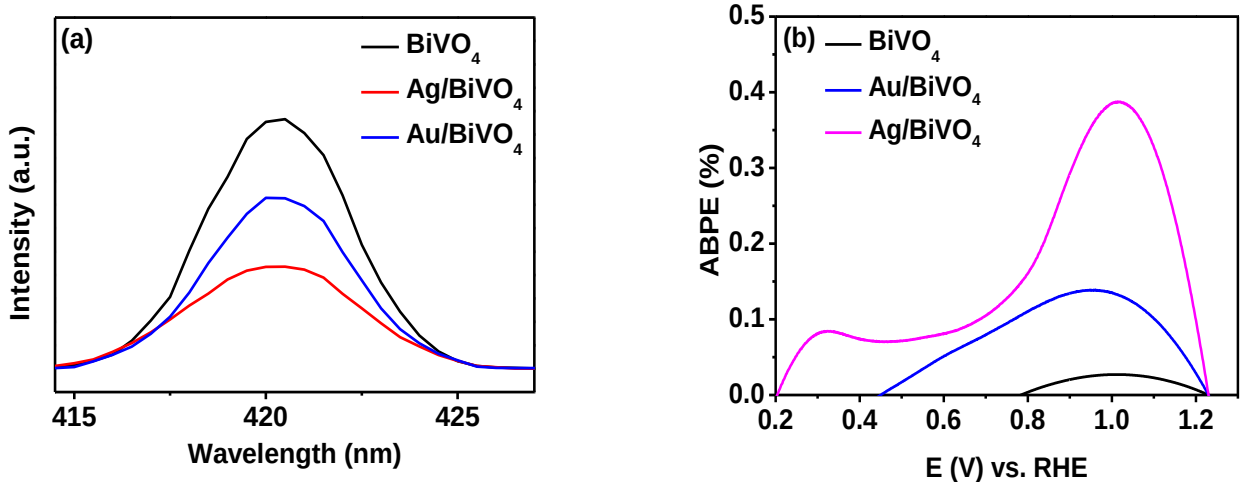

Figure 10. (**a**) Photoluminescence (PL) spectra and (**b**) applying bias photon current efficiency (ABPE) curves of $NM/BiVO_4$.

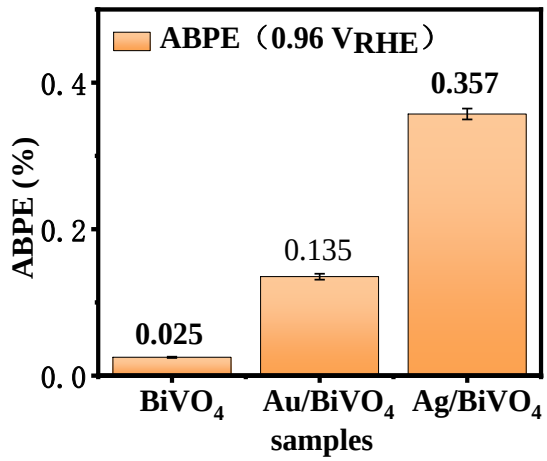

Figure 11. Standard deviation of ABPE of the sample tested 5 times at 0.96 V_{RHE}.

The charge transfer kinetics at the interface can be unambiguously analyzed using the Nyquist plots of EIS, as shown in Figure 12a. The circuit is shown in the picture, where R_{CT} represents charge transfer resistance at the electrode/electrolyte interface, and R_S represents the series resistance [32]. The information conveyed by the Nyquist curve is that the smaller the radius of the curves, the lower is the impedance of the samples [33]. Therefore, the impedance of $Ag/BiVO_4$ was the lowest and the impedance of $BiVO_4$ was the highest in all samples. It follows that after $BiVO_4$ is compounded with NM, the electrical conductivity and the charge-specific efficiency at the electrode/electrolyte interface are also

enhanced. It can be seen from Figure 12b that the surface photovoltage (SPV) relationship of the samples is as follows: $Ag/BiVO_4$ > $Au/BiVO_4$ > $BiVO_4$. The generation range of SPV is consistent with the UV-vis absorption range. The above results were consistent with previous experimental results. The compound of two noble metal nanoparticles improves the photoelectrochemical performance of $BiVO_4$.

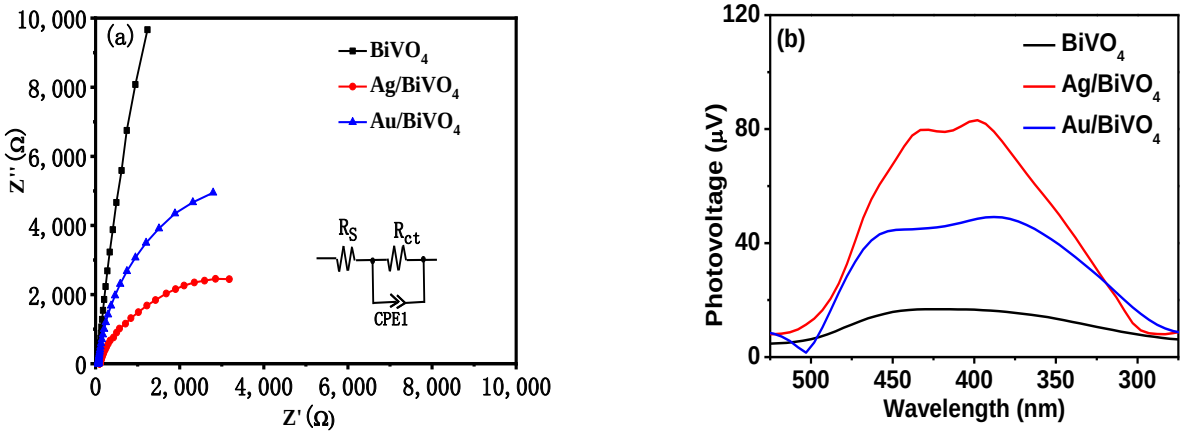

Figure 12. (**a**) The Nyquist curves of EIS for $BiVO_4$, $Ag/BiVO_4$, and $Au/BiVO_4$. (**b**) SPV curves of samples.

The photoelectric catalytic water splitting experiments of different samples for hydrogen production are shown in Figure 13. The results of the quantitative detection performed using gas chromatography are displayed in Figure 13a. It can be seen that at the fifth hour, the hydrogen evolution of pure $BiVO_4$ is about 1.10 μmol·cm^{-2}. $Ag/BiVO_4$ and $Au/BiVO_4$ are 3.56 and 2.32 times pure $BiVO_4$, respectively. Figure 12b shows the average hydrogen evolution rate, where the hydrogen evolution rate of pure $BiVO_4$ is the lowest. Figure 13a,b show the oxygen evolution and average oxygen evolution rate of the photoanodes. The results are consistent with hydrogen evolution. Therefore, the results confirm that the loading of noble metal nanoparticles can improve the hydrogen evolution rate. Ag NPS and Au NPs with SPR effect can absorb large wavelengths of visible light and inhibit the recombination of holes and electrons, increasing the hydrogen evolution. Ag NPs exhibited higher hydrogen evolution than Au NP modified $BiVO_4$ because the work function of Ag and Au was 4.26 eV [34] and 5.1 eV, respectively, while the work function of $BiVO_4$ was 4.8 eV. The hot electrons generated in Ag NPs could transfer from Ag NPs to $BiVO_4$ more smoothly. Hot electrons generated by Au will overcome more electron barriers and flow into $BiVO_4$, resulting in a decline in PEC performance compared with $Ag/BiVO_4$. Combined with more reactive sites and stronger SPR effect provided by Ag NPs, it was effectively proved that Ag NP modified $BiVO_4$ showed higher hydrogen production activity.

Combining the above characterization analysis and experimental results, Figure 14 shows the working mechanism of $NM/BiVO_4$. Under irradiation, NM NPs produce the SPR effect and are excited to produce "hot electrons", which can directly enter the CB of $BiVO_4$ through the electron transfer mechanism and participate in photocathode reduction reaction together with photogenerated electrons. At the same time, the NM NPs surface generates electromagnetic fields, and "hot electrons" generate potential energy at the metal-semiconductor interface. It was confirmed that a Schottky barrier is generated when the NM NPs are in contact with $BiVO_4$. The potential energy generated by the Schottky barrier is smaller than that generated by the "hot electrons" at the contact interface, which enables the "hot electrons" to be smoothly transferred from the NM NPs to $BiVO_4$. The Schottky barrier can keep the "hot electrons" generated by NM NPs in the CB of $BiVO_4$ and not return them to the NM NPs. Therefore, the recombination of noble metals with the SPR effect can enhance the recombination of carriers and improve the charge transfer efficiency of $BiVO_4$.

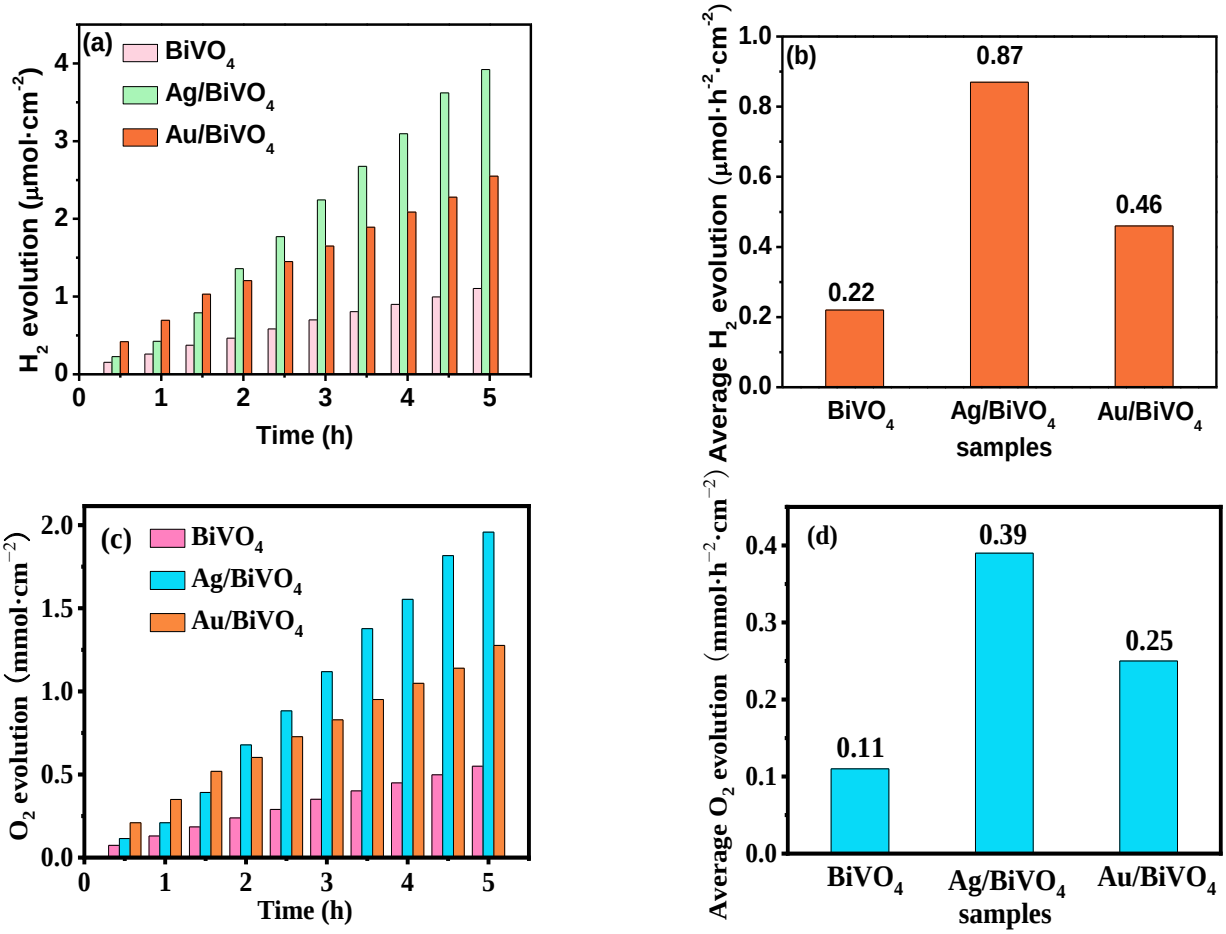

Figure 13. (**a**) Hydrogen evolution amount, (**b**) average hydrogen evolution rate, (**c**) oxygen evolution amount, and (**d**) average oxygen evolution rate of the samples under AM 1.5 G continuous illumination.

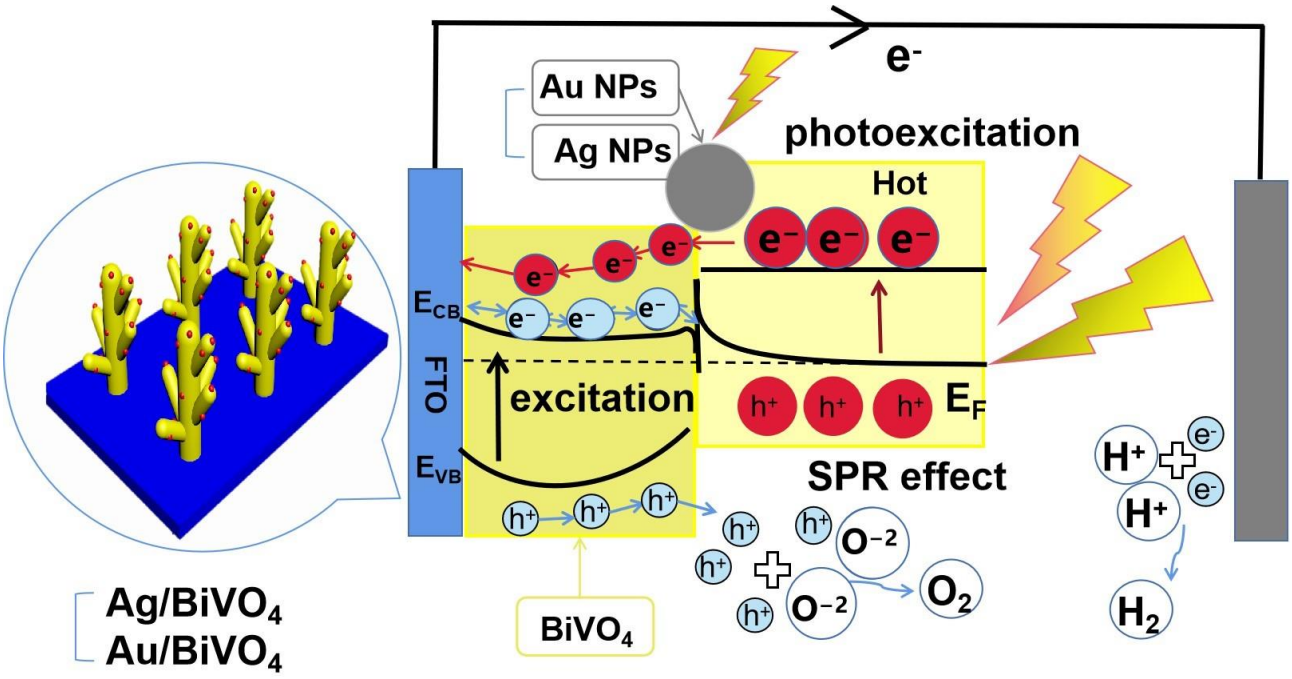

Figure 14. Schematic diagram of hydrogen production of NM/$BiVO_4$.

3. Conclusions

The paper proposes a new idea of loading several types of noble metal nanoparticles on $BiVO_4$, while the PEC performances of the $BiVO_4$-loaded NM NPs were investigated. The photocurrent density values of photoanode Ag/$BiVO_4$ and Au/$BiVO_4$ are 3.82 and 1.72 times that of pure $BiVO_4$, respectively. In addition, when Ag/$BiVO_4$ and Au/$BiVO_4$ are used as photoanodes, the hydrogen evolution of the counter electrodes is 3.56 and 2.32 times that of pure $BiVO_4$ as a photoanode under AM 1.5 G continuous illumination. $BiVO_4$ modification with NM NPs effectively improves the performance of PEC. The SPR effect exhibited by NM NPs can broaden the absorption range of visible light, effectively capture photogenerated electrons, and increase the concentration of charge carriers, resulting in faster carrier separation rate and interface charge transfer efficiency. However, compared to Au/$BiVO_4$, Ag/$BiVO_4$ has higher light absorption, higher photocurrent, and greater oxygen evolution. This can be explained by the fact that Ag NPs are exposed to more active sites, with a stronger SPR effect, and a smaller electronic barrier, so that Ag/$BiVO_4$ also shows higher PEC activity. In conclusion, NM NPs modified $BiVO_4$ can show excellent PEC performance, which is an effective way to enhance the PEC performance of $BiVO_4$.

4. Experimental Section

4.1. Synthesis of $BiVO_4$ Films

The monoclinic $BiVO_4$ was prepared by the method studied by predecessors [35]. First, prepare solution A, dissolve 0.04 M $Bi(NO_3)_3$ solution in 0.4 M KI aqueous solution, and add concentrated HNO_3 to adjust the pH to about 1.75. Then prepare solution B; mix 20 mL of ethanol solution with 0.23 M p-benzoquinone. Mix A and B to get solution C. Electrodeposition BiOI films were performed at a potential of −0.143 V vs. SCE for 600 s using a three-electrode electrochemical with C solution as the electrodeposition solution, a fluorine-doped tin oxide (FTO) as working electrode, platinum sheet as the counter electrode, and Ag/AgCl as the reference electrode. Put the prepared BiOI into an oven at 60 °C to dry for 5 h. Afterwards, prepare solution D; solution D consists of 50 mL DMSO and 0.2 M $VO(acac)_2$. The prepared solution D was dropped onto BiOI, and then it was dried and annealed. Annealing conditions were 450 °C (The temperature rose by 2 °C/min) for 2 h. Finally, there was excess V_2O_5 on the annealed samples, so after soaking the samples in 1 M NaOH for 30 min, the desired $BiVO_4$ electrode was obtained after drying.

4.2. Fabrication of Ag/$BiVO_4$ and Au/$BiVO_4$ Photoanodes

Fabrication of Ag/$BiVO_4$ photoanodes: Prepare a solution by mixing 2.00 mM, 2.50 mM, and 3.00 mM $AgNO_3$ and 1 mM $C_6H_5Na_3O_7$, respectively, denoted as Ag_2/$BiVO_4$, $Ag_{2.5}$/$BiVO_4$, and Ag_3/$BiVO_4$. The $BiVO_4$-coated FTO substrate is then immersed in the mixed solution and transferred to a hydrothermal reactor at 100 °C for 2 h.

Fabrication of Au/$BiVO_4$ photoanodes: 2.50 mM $HAuCl_4$ was used as the electrodeposition solution, and $BiVO_4$ was used as the working electrode to deposit at a potential of 0.10 V vs. SCE for 100 s, 150 s, and 200 s, denoted as Au_{100}/$BiVO_4$, Au_{150}/$BiVO_4$, and Au_{200}/$BiVO_4$, respectively.

Author Contributions: Conceptualization, R.L., C.H. and Z.-Q.L.; methodology, R.L.; software, R.L.; validation, R.L., D.Z. and D.W.; formal analysis, R.L.; investigation, R.L., H.Z. and Z.M.; resources, R.L. and Q.F.; data curation, R.L. and Z.-Q.L.; writing—original draft preparation, R.L.; writing—review and editing, R.L. and H.Z.; visualization, C.H.; supervision, C.H.; project administration, C.H.; funding acquisition, C.H. All authors have read and agreed to the published version of the manuscript.

Funding: This research was funded by the National Natural Science Foundation of China grant number 52103339 and the Natural Science Foundation of Hubei Province grant number 2018CFB282.

Data Availability Statement: Not applicable.

Conflicts of Interest: The authors declare no conflict of interest.

References

1. Chen, D.; Liu, Z.F.; Guo, Z.G.; Yan, W.G.; Xin, Y. Enhancing light harvesting and charge separation of Cu_2O photocathodes with spatially separated noble-metal cocatalysts towards highly efficient water splitting. *J. Mater. Chem. A* **2018**, *6*, 20393–20401. [CrossRef]
2. Wang, Z.; Li, C.; Domen, K. Recent developments in heterogeneous photocatalysts for solar-driven overall water splitting. *Chem. Soc. Rev.* **2019**, *48*, 2109–2125. [CrossRef] [PubMed]
3. Wang, W.H.; Qi, L.M. Light Management with patterned micro- and nanostructure arrays for photocatalysis, photovoltaics, and optoelectronic and optical devices. *Adv. Funct. Mater.* **2019**, *29*, 1807275. [CrossRef]
4. Tilley, S.D. Recent advances and emerging trends in photoelectrochemical solar energy conversion. *Adv. Energy Mater.* **2019**, *9*, 1802877. [CrossRef]
5. Feng, J.N.; Bian, J.; Bai, L.L.; Xi, S.B.; Wang, Y.; Chen, C.L.; Jing, L.Q. Efficient wide-spectrum photocatalytic overall water splitting over ultrathin molecular nickel phthalocyanine/$BiVO_4$ Z-scheme heterojunctions without noble metals. *Appl. Catal. B Environ.* **2021**, *295*, 120260. [CrossRef]
6. Zheng, C.Y.; Yin, M.M.; Ge, R.; Wei, J.; Su, B.Y.; Chen, X.; Chen, X.M. Competitive near-infrared PEC immunosorbent assay for monitoring okadaic acid based on a disposable flower-like WO_3-Modified screen-printed electrode. *Biosens. Bioelectron.* **2021**, *185*, 113278. [CrossRef]
7. Dou, Y.B.; Zhou, J.; Zhou, A.; Li, J.R.; Nie, Z.R. Visible-light responsive MOF encapsulation of noble-metal-sensitized semiconductors for high-performance photoelectrochemical water splitting. *J. Mater. Chem.* **2017**, *5*, 19491. [CrossRef]
8. Zhou, T.S.; Chen, S.; Wang, J.C.; Zhang, Y.; Li, J.H.; Bai, J.; Zhou, B.X. Dramatically enhanced solar-driven water splitting of $BiVO_4$ photoanode via strengthening hole transfer and light harvesting by co-modification of CQDs and ultrathin beta-FeOOH layers. *Chem. Eng. J.* **2021**, *403*, 126350. [CrossRef]
9. Hernández-Alonso, M.D.; Fresno, F.; Suárez, S.; Coronado, J.M. Development of alternative photocatalysts to TiO_2: Challenges and opportunities. *Energy Environ. Sci.* **2009**, *2*, 1231–1257. [CrossRef]
10. Son, M.K.; Pan, L.F.; Mayer, M.T.; Hagfeldt, A.; Gratzel, M.; Luo, J.S. Structural and compositional investigations on the stability of cuprous oxide nanowire photocathodes for photoelectrochemical water splitting. *ACS Appl. Mater. Interfaces* **2021**, *13*, 55080–55091. [CrossRef]
11. Luo, W.J.; Yang, Z.S.; Li, Z.S.; Zhang, J.Y.; Liu, J.G.; Zhao, Z.Y.; Wang, Z.Q.; Yan, S.C.; Yu, T.; Zou, Z.G. Solar hydrogen generation from seawater with a modified $BiVO_4$ photoanode. *Energy Environ. Sci.* **2011**, *4*, 4046–4051. [CrossRef]
12. Wu, J.M.; Chen, Y.; Pan, L.; Wang, P.H.; Cui, Y.; Kong, D.C.; Wang, L.; Zhang, X.W.; Zou, J.J. Multi-layer monoclinic $BiVO_4$ with oxygen vacancies and V^{4+} species for highly efficient visible-light photoelectrochemical applications. *Appl. Catal. B Environ.* **2018**, *221*, 187–195. [CrossRef]
13. Ye, K.Y.; Chai, Z.S.; Gu, J.W.; Yu, X.; Zhao, C.X.; Zhang, Y.M.; Mai, W.J. BiOI-$BiVO_4$ photoanodes with significantly improved solar water splitting capability: P-n junction to expand solar adsorption range and facilitate charge carrier dynamics. *Nano Energy* **2015**, *18*, 222–231. [CrossRef]
14. Li, J.Q.; Guo, Z.Y.; Liu, H.; Du, J.; Zhu, A.F. Two-step hydrothermal process for synthesis of F-doped $BiVO_4$ spheres with enhanced photocatalytic activity. *J. Alloys Compd.* **2013**, *581*, 40–45. [CrossRef]
15. Wang, S.G.; Chen, P.; Bai, Y.; Yun, J.H.; Liu, G.; Wang, L.Z. New $BiVO_4$ dual photoanodes with enriched oxygen vacancies for efficient solar-driven water splitting. *Adv. Mater.* **2018**, *30*, 1800486. [CrossRef]
16. Thalluri, S.M.; Hernández, S.; Bensaid, S.; Saracco, G.; Russo, N. Green-synthesized W and Mo-doped $BiVO_4$ oriented along the 040 facet with enhanced activity for the sun-driven water oxidation. *Appl. Catal. B Environ.* **2016**, *180*, 630–636. [CrossRef]
17. Liu, R.; Wang, D.; Han, C.C.; Wang, P.; Tong, Z.F.; Tan, B.H.; Liu, Z.F. The synergistic effect of $CuBi_2O_4$ and Co-Pi: Improving the PEC activity of $BiVO_4$-based composite materials. *New J. Chem.* **2022**, *46*, 2971–2979. [CrossRef]
18. Fang, G.Z.; Liu, Z.F.; Han, C.C. Enhancing the PEC water splitting performance of $BiVO_4$ co-modifying with NiFeOOH and Co-Pi double layer cocatalysts. *Appl. Surf. Sci.* **2020**, *515*, 146095. [CrossRef]
19. Geng, H.M.; Ying, P.Z.; Zhao, Y.L.; Gu, X.Q. Cactus shaped FeOOH/Au/$BiVO_4$ photoanodes for efficient photoelectrochemical water splitting. *Int. J. Hydrogen Energy* **2021**, *46*, 35280–35289. [CrossRef]
20. Su, F.L.; Wang, T.; Lv, R.; Zhang, J.J.; Zhang, P.; Lu, J.W.; Gong, J.L. Dendritic Au/TiO_2 nanorod arrays for visible-light driven photoelectrochemical water splitting. *Nanoscales* **2013**, *5*, 9001–9009. [CrossRef]
21. Nga, T.T.T.; Huang, Y.C.; Chen, J.L.; Chen, C.L.; Lin, B.H.; Yeh, P.H.; Du, C.H.; Chiou, J.W.; Pong, W.F.; Arul, K.T.; et al. Effect of Ag-decorated $BiVO_4$ on photoelectrochemical water splitting: An X-ray absorption spectroscopic investigation. *Nanomaterials* **2022**, *12*, 3659. [CrossRef] [PubMed]
22. Li, M.; Tu, X.L.; Su, Y.J.; Lu, J.; Hu, J.; Cai, B.F.; Zhou, Z.H.; Yang, Z.; Zhang, Y.F. Controlled growth of vertically aligned ultrathin In_2S_3 nanosheet arrays for photoelectrochemical water splitting. *Nanoscale* **2018**, *10*, 1153–1161. [CrossRef] [PubMed]
23. Kim, J.H.; Jo, Y.H.; Kim, J.H.; Lee, J.S. Ultrafast fabrication of highly active $BiVO_4$ photoanodes by hybrid microwave annealing for unbiased solar water splitting. *Nanoscale* **2016**, *8*, 17623–17631. [CrossRef] [PubMed]
24. Myung, N.; Ham, S.; Choi, S.; Chae, Y.; Rajeshwar, K. Tailoring interfaces for electrochemical synthesis of semiconductor films: $BiVO_4$, Bi_2O_3, or composites. *J. Phys. Chem. C* **2011**, *115*, 7793–7800. [CrossRef]
25. Gu, X.N.; Zhang, J.L.; Hou, L.Q.; Fu, X.H.; Yu, X.; Zhu, Y.; Zhang, Y.M. Dual modification with Ag and FeOOH significantly increased the photoelectrochemical water splitting activity of $BiVO_4$ photoanodes. *Surf. Interfaces* **2021**, *25*, 101224. [CrossRef]

26. Gao, X.T.; Bai, Z.Q.; Zhang, S.; Liu, J.C.; Li, Z.H. Highly efficient hamburger-like nanostructure of a triadic $Ag/Co_3O_4/BiVO_4$ photoanode for enhanced photoelectrochemical water oxidation. *RSC Adv.* **2020**, *10*, 45067. [CrossRef]
27. Zhang, L.; Herrmann, L.O.; Baumberg, J.J. Size dependent plasmonic effect on $BiVO_4$ photoanodes for solar water splitting. *Sci. Rep.* **2015**, *5*, 16660. [CrossRef]
28. Lim, F.S.; Tan, S.T.; Zhu, Y.M.; Chen, J.W.; Wu, B.; Yu, H.; Kim, J.M.; Ginting, R.T.; Lau, K.S.; Chia, C.H.; et al. Tunable plasmon-induced charge transport and photon absorption of bimetallic Au-Ag nanoparticles on ZnO photoanode for photoelectrochemical enhancement under visible light. *J. Phys. Chem.* **2020**, *124*, 14105–14117. [CrossRef]
29. Linic, S.; Christopher, P.; Ingram, D.B. Plasmonic-metal nanostructures for efficient conversion of solar to chemical energy. *Nat. Mater.* **2011**, *10*, 911–921. [CrossRef]
30. Walter, M.G.; Warren, E.L.; Mckone, J.R.; Boettcher, S.W.; Lewis, N.S. Solar water splitting cells. *Chem. Rev.* **2010**, *110*, 6446–6473. [CrossRef]
31. Tian, Y.; Cui, Q.Q.; Xu, L.L.; Jiao, A.X.; Ma, H.; Wang, C.; Zhang, M.Y.; Wang, X.L.; Li, S.; Chen, M. Alloyed AuPt nanoframes loaded on h-BN nanosheets as an ingenious ultrasensitive near-infrared photoelectrochemical biosensor for accurate monitoring glucose in human tears. *Biosens. Bioelectron.* **2021**, *192*, 113490. [CrossRef] [PubMed]
32. Long, X.F.; Gao, L.L.; Li, F.; Hu, Y.P.; Wei, S.Q.; Wang, C.L.; Wang, T.; Jin, J.; Ma, J.T. Bamboo shoots shaped $FeVO_4$ passivated ZnO nanorods photoanode for improved charge separation/transfer process towards efficient solar water splitting. *Appl. Catal. B Environ.* **2019**, *257*, 117813. [CrossRef]
33. Nan, F.; Kang, Z.; Wang, J.; Shen, M.; Fang, L. Carbon quantum dots coated $BiVO_4$ inverse opals for enhanced photoelectrochemical hydrogen generation. *Appl. Phys. Lett.* **2015**, *106*, 153901–153905. [CrossRef]
34. Jiao, Z.; Zhang, Y.; Ouyang, S.; Yu, H.; Lu, G.; Ye, J.; Bi, Y. BiAg alloy nanospheres: A new photocatalyst for H_2 evolution from water splitting. *ACS Appl. Mater. Interfaces* **2014**, *6*, 19488–19493. [CrossRef]
35. Kim, T.W.; Choi, K.S. Nanoporous $BiVO_4$ photoanodes with dual-layer oxygen evolution catalysts for solar water splitting. *Science* **2014**, *343*, 990–994. [CrossRef]